Gramsch et al. *Journal of Mathematics in Industry* (2016) 6:13
DOI 10.1186/s13362-016-0034-4

Journal of Mathematics in Industry
a SpringerOpen Journal

RESEARCH Open Access

Aerodynamic web forming: process simulation and material properties

Simone Gramsch[1], Axel Klar[2], Günter Leugering[3], Nicole Marheineke[3*], Christian Nessler[2], Christoph Strohmeyer[3] and Raimund Wegener[1]

*Correspondence:
nicole.marheineke@fau.de
[3]Department Mathematik, FAU Erlangen-Nürnberg, Cauerstr. 11, Erlangen, 91058, Germany
Full list of author information is available at the end of the article

Abstract

In this paper we present a chain of mathematical models that enables the numerical simulation of the airlay process and the investigation of the resulting nonwoven material by means of virtual tensile strength tests. The models range from a highly turbulent dilute fiber suspension flow to stochastic surrogates for fiber lay-down and web formation and further to Cosserat networks with effective material laws. Crucial is the consistent mathematical mapping between the parameters of the process and the material. We illustrate the applicability of the model chain for an industrial scenario, regarding data from computer tomography and experiments. By this proof of concept we show the feasibility of future simulation-based process design and material optimization which are long-term objectives in the technical textile industry.

MSC: 65Mxx; 74Hxx; 74Kxx; 74Q15; 76T20

Keywords: airlay process; nonwoven material; virtual tensile strength test; fiber suspension flow; fiber lay-down; fiber networks; model chain; stochastic surrogates; homogenization; effective material laws

1 Introduction

Aerodynamic web forming addresses a broad spectrum of applications for the produced nonwoven materials. Airlay fabrics range from insulation and filter materials over automotive and mattress felts to medical and hygiene products depending on the type of entering fiber material (e.g., natural (cotton, flax, hemp, etc.), man-made fibers or even reclaimed textile waste). The fibers may have a length up to 120 mm and a weight between 1 and 200 dtex (1 dtex = 10^{-7} kg/m). In the airlay process the fibers leave from a rotating drum into a turbulent air flow. Suctioning onto a perforated moving conveyor belt leads to the forming of a random three-dimensional web structure, see Figure 1 and [1]. The production of the final fabrics takes place in further post-processing steps. Simulation-based process design and management are a basis for the prediction and improvement of product properties and an objective in industry. This requires the mathematical modeling of the process which is topic of the paper.

The aerodynamic web forming is a multi-scale two-phase problem whose monolithic handling and direct simulation based on a model of first principles are not possible due to its high complexity. So far, no simulation results exist in literature. In this paper, we establish a consistent, accurate and efficiently evaluable chain of mathematical models

Figure 1 Industrial production of airlay fabrics. *From left to right*: Airlay machine (Airlay-K12 by machine manufacturer AUTEFA Solutions), aerodynamic web forming, nonwoven material.

towards the simulation of the airlay process and furthermore the investigation of the material behavior. The models cover the dilute fiber suspension with elastic slender bodies in the turbulent flow, stochastic surrogates for the fiber lay-down and web formation as well as Cosserat networks with effective material laws for tensile strength tests. They are coupled by means of parameter identification. We illustrate the applicability of the model chain for an industrial set-up, regarding computer tomography data and tensile strength experiments of the airlay nonwoven materials.

The promising use of model hierarchies and model chains for the virtual production of filaments and nonwovens in the technical textile industry is topic in [2]. A model hierarchy for nonwoven manufacturing in the spunbond process was presented in [3], we adapt and transfer the ideas for the handling of the endless fibers in the respective entanglement and deposition regimes to the staple fibers in the airlay process at hand. The simulation of elastic fibers in the turbulent flow is performed on the works [4, 5], using an inextensible Kirchhoff beam model that is capable of large, geometrically nonlinear deformations and driven by a stochastic aerodynamic drag force. Presupposing a statistic turbulence model for the flow field, the turbulence impact on the fiber dynamics is described by a Gaussian white noise with a flow-dependent amplitude that carries the information of kinetic turbulent energy, dissipation rate, and correlation structure. Due to the huge amount of physical details such simulations are computationally extremely costly and practically limited to some hundreds of fibers. This motivates the introduction of a stochastic surrogate for the virtual web generation: a lay-down model describes the fiber position on the conveyor belt. Containing parameters that characterize the process, it is calibrated by means of a representative sample of dynamical fiber-flow simulations and allows for the fast and efficient computation of a web with millions of fibers. We refer to [6, 7] for lay-down models of endless fibers (2D/3D, isotropic/anisotropic, smooth/standard), to [8–10] for their analysis regarding ergodicity and existence results and to [11] for a comparison with computer tomography data for spunbond materials. Using the random topology generated by the lay-down model we design the elastic microstructure via Cosserat networks based on beams and trusses. Homogenization techniques allow for modeling effective material laws and investigating the tensile strength in dependence on characterizing net parameters. Stochastic fiber networks and non-periodic homogenization are a recent topic of research and were addressed in, e.g., [12–15]. For an homogenization approach on nonwoven materials see [16], this article also provides a remarkable survey over nonwoven microstructure models and studies in literature. Model- and simulation-based investigations of the tensile behavior and mechanical analysis of nonwoven materials can be found in, e.g., [16–18] and [19].

Table 1 Structure of the paper based on model chain

process simulation	→	**microstructure generation**	→	**material investigation**
fiber suspension flow dynamics and deposition *Section* 2		stochastic fiber lay-down model elastic Cosserat network *Section* 3		virtual tensile strength test effective material laws *Section* 4

Structure of the paper. The structure of the paper reflects the three relevant modeling steps concerning the fiber-loaded turbulent flow simulation (Section 2), the microstructure generation (Section 3) and the effective material description and investigation (Section 4), cf. Table 1. All models - apart from the surrogate fiber lay-down model - are originated in the framework of fluid dynamics and solid mechanics, describing well-known conservation properties in form of (partial, ordinary, stochastic) differential equations. In spite of the similar background each model by itself is extensive and rich in variables and parameters. To handle the accompanying complexity in notation and to facilitate the readability of the paper, each section is organized in the same way: we present the single model, whereat numerical or algorithmic details are given in separate paragraphs. Embedding it into the model chain we explain its coupling with the other models and - as an example - we apply it to the industrial airlay process scenario that is specified in Section 1.1 as reference case. Ending with integrated simulation results from process to material we conclude with a discussion on the sensitivity of the parameters and an outlook to future optimization issues in Section 5.

1.1 Industrial airlay process, reference scenario

A typical airlay process with the rotating card cylinder, the aerodyamic web forming zone and the conveyor belt is sketched in Figure 2. For the process description we introduce a fixed Cartesian coordinate system $\{\mathbf{e_x}, \mathbf{e_y}, \mathbf{e_z}\}$ in $\mathbb{R}^3$ with respect to the machinery, whose origin is centered on the conveyor belt below the fibers' dropping. We refer to the machine direction (MD) $\mathbf{e_x}$ and its cross direction (CD) $\mathbf{e_y}$, where the conveyor belt lies in the MD-CD plane ($z = 0$). The associated MD and CD cut planes are given by $y = \text{const}$ and $x = \text{const}$, respectively. Apart from boundary effects the process properties are homogeneous in CD. In this paper we consider the industrial airlay plant K12 by the machine manufacturer AUTEFA Solutions (Figure 1) with which the following reference scenario has been studied. As entering fiber material a mixture of 70% solid PES fibers and 30% bicomponent fibers whose core is made from PES and whose surface is made from PET at a ratio of 1 : 1 is considered. The mixing ratios refer to the mass. The fibers are homogeneous with circular cross-sections, their properties are summarized in Table 2. The airlay machine is run with a mass rate $\dot{m}$ of 0.0481 kg/s, the card cylinder rotates with an angular speed v_C of 199 s^{-1}, and the conveyor belt with a width b of 2.4 m moves with a speed v_B of 0.0333 m/s. The produced nonwoven has a base weight W of 0.6 kg/m^2 and a height H of 0.06 m. In post-processing the nonwoven material is reinforced by thermobonding where the bicomponent fibers have an adhesive effect. The tensile strength experiments are performed on the thermobonded nonwoven regarding DIN-norm (GME 60349). Note that all quantities are given in SI-units in this paper.

Notation 1 Throughout this paper we typeset vector- and tensor-valued quantities in small and large boldfaced letters, respectively. Scalars are normal-typed, we especially indicate the scalar parameters specified for the industrial reference scenario (Section 1.1) by

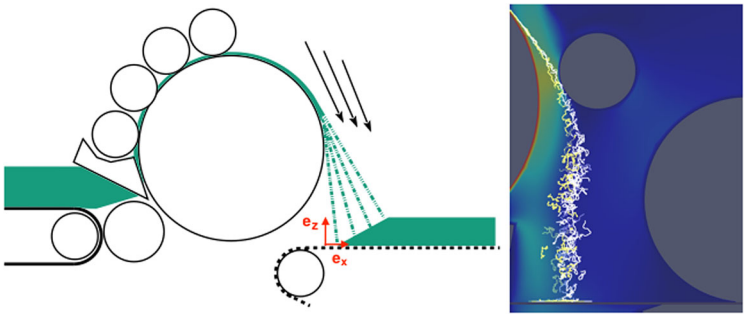

Figure 2 Airlay process. *Left*: Sketch of the process. *Right*: Illustration of the aerodynamic web forming zone with fiber-loaded flow in the considered K12-plant geometry (MD cut plane). Machine parts, i.e., rotating card cylinder, conveyor belt as well as baffle pipe and pressing roll, are displayed in grey, simulated single fibers are visualized in front of the air flow that is colored by the mean velocity magnitude, cf. Section 2.2.

Table 2 Fiber properties in reference scenario

Property	Symbol	Unit	Bico fiber (PES/PET)	Solid fiber (PES)
Line density, titer	$(\rho \mathrm{A})$	kg/m	$4.4 \cdot 10^{-7}$	$6.7 \cdot 10^{-7}$
Density	ρ	kg/m^3	$1.325 \cdot 10^{+3}$	$1.38 \cdot 10^{+3}$
Diameter	D	m	$2.1 \cdot 10^{-5}$	$2.5 \cdot 10^{-5}$
Length (straight | crimped)	$\mathrm{L} \mid \ell$	m	$6.0 \mid 5.1 \cdot 10^{-2}$	$6.0 \mid 5.1 \cdot 10^{-2}$
Crimp number	C	bow/m	$7 \cdot 10^{+2}$	$5 \cdot 10^{+2}$
Elasticity modulus	E	N/m^2	$3 \cdot 10^{+9}$	$3 \cdot 10^{+9}$
Shear modulus	G	N/m^2	$1.035 \cdot 10^{+9}$	$1.035 \cdot 10^{+9}$
Bending stiffness	(EI)	Nm^2	$2.6 \cdot 10^{-11}$	$5.6 \cdot 10^{-11}$
Tensile strength	S	N/(kg/m)	$3.3 \cdot 10^{+5}$	$3.0 \cdot 10^{+5}$

a Roman font. Sets are denoted by caligraphic letters. We use a tensor calculus with the dot operator $\cdot$ and the tensor product $\otimes$.

2 Process simulation

The core of the aerodynamic web forming is the dilute suspension behavior of flexible fibers in the turbulent flow. The random microstructure is essentially determined by the fibers' deposition, i.e., the distribution of the fibers on the conveyor belt as well as their characteristic geometrical lay-down properties. The fiber-loaded turbulent flow is a multi-scale two-phase problem in a complex geometry. Direct numerical simulation based on the model of first principles as well as approaches like immersed boundary or fictitious boundary/domain are well investigated for fluid-structure problems, but their applicability is practically limited to laminar flows and a small number of suspended solids due to the required high computational demands (from the broad existing literature see, e.g., [20–26]). For flows with a high particle load kinetic modeling approaches have been established, leading to coupled Navier-Stokes Fokker-Planck systems (see the monographs [27, 28] and reference therein). However, these approaches do not cover flexible fibers with infinitely many degrees of freedom. In this work we follow [2, 5] and model a fiber asymptotically as elastic Kirchhoff beam that is capable of large, geometrically nonlinear deformations and driven by a stochastic aerodynamic drag force due to the surrounding turbulent flow field. The flow is specified by a statistic k-ϵ turbulence model. Because of the low load concentration in the airlay process we neglect fiber-fiber interactions as well as the fibers' impact on the turbulent flow.

2.1 Elastic fiber dynamics in turbulent flows

Let $\Omega \subset \mathbb{R}^3$ be the flow domain with boundary $\partial\Omega$, $\overline{\Omega} = \Omega \cup \partial\Omega$. According to the Cosserat theory [29] a slender fiber can be asymptotically represented by a time-dependent curve (e.g., its center-line) $\mathbf{r} : \mathcal{I} \times \mathbb{R}_0^+ \to \overline{\Omega}$ with material parameter $s \in \mathcal{I} = [0, \ell]$ and time $t \in \mathbb{R}_0^+$. Its dynamics due to inertia and bending, driven by turbulence can be described for fiber curve, velocity and tangential traction $(\mathbf{r}, \mathbf{v}, N)$ by the following constrained partial differential equations with multiplicative Gaussian space-time noise [3, 5]

$$\partial_t \mathbf{r} = \mathbf{v}, \qquad \|\partial_s \mathbf{r}\| = 1, \tag{2.1a}$$

$$(\rho \mathrm{A})\partial_t \mathbf{v} = \partial_s\big(N\partial_s \mathbf{r} - \partial_s\big((\mathrm{EI})\partial_{ss}\mathbf{r}\big)\big) + \mathbf{f}(\mathbf{r}, \mathbf{v}, \partial_s \mathbf{r}; \mathbf{u}) + \mathbf{A}(\mathbf{r}, \mathbf{v}, \partial_s \mathbf{r}; \mathbf{u}, k, \epsilon) \cdot \partial_{st}\mathbf{w}, \tag{2.1b}$$

supplemented with appropriate initial and boundary conditions, where $(\rho\mathrm{A})$ and (EI) denote the fiber line density (titer) and bending stiffness. The unknown traction $N : \mathcal{I} \times \mathbb{R}_0^+ \to \mathbb{R}$ is the Lagrange multiplier to the pointwise inextensibility constraint in the Euclidean norm $\|\cdot\|$ (2.1a). The corresponding deterministic system is known as Kirchhoff beam (or Kirchhoff-Love equations), it results from the Cosserat rod model in the asymptotic limit when the slenderness parameter and the typical Mach number vanish [30]. Crucial for the dynamic fiber behavior are the aerodynamic drag forces that depend locally on the angle of attack (fiber tangent) and the relative velocity between fluid flow and fiber. Applying the stochastic force model by [5], we presuppose an underlying statistic k-ϵ turbulence description that provides the mean flow velocity $\mathbf{u} : \overline{\Omega} \times \mathbb{R}_0^+ \to \mathbb{R}^3$. Additionally, it characterizes the turbulent flow fluctuations by the kinetic turbulent energy k and the dissipation rate ϵ, i.e., $k, \epsilon : \overline{\Omega} \times \mathbb{R}_0^+ \to \mathbb{R}$. The drag forces are composed of the mean $\mathbf{f}$ in a parametric dependence on the mean flow velocity $\mathbf{u}$ evaluated at $(\mathbf{r}, t)$ and of a fluctuating part. The fluctuations are particularly modeled as Gaussian space-time white noise with the vector-valued Wiener process ($\mathbf{w} : \mathcal{I} \times \mathbb{R}_0^+ \to \mathbb{R}^3$) and the tensor-valued amplitude $\mathbf{A}$ that carries the correlation structure of the turbulence via a parametric dependence on the flow quantities $\mathbf{u}$, k and ϵ. For details we refer to [5]. Arising contacts of the fiber with the geometry are realized by means of nonholonomic constraints. Let $\Gamma \subset \partial\Omega$ denote the domain boundary with walls. We introduce a signed distance function $h(\cdot, t) \in \mathcal{C}^2(\mathbb{R}^3, \mathbb{R})$, satisfying $h = 0$ in Γ and $h > 0$ in Ω for all $t \geq 0$. Then, the momentum balance (2.1b) becomes

$$(\rho \mathrm{A})\partial_t \mathbf{v} = \cdots + \lambda \frac{\nabla h}{\|\nabla h\|}, \qquad (\lambda = 0 \wedge h > 0) \vee (\lambda > 0 \wedge h = 0) \tag{2.1c}$$

with the associated Lagrange multiplier λ. Here, $\cdots$ represents the whole of the right-hand side of (2.1b). For modeling a fiber's deposition the contact approach can be combined with a Coulomb friction model (kinetic and dynamic), in which λ acts as normal force according to its physical significance.

Numerical treatment. Fiber-flow computations at industrial scale require a highly efficient numerical performance. We use the commercial CFD software[a] ANSYS Fluent for the flow and the licensable research software[b] FIDYST for the fiber simulations.

The numerics of the constrained stochastic fiber system (2.1a)-(2.1c) is based on a spatial semi-discretization with finite volumes, in which $\mathbf{r}$ and $\mathbf{v}$ are assigned to the cell nodes, but N, and consequently also the inextensibility constraint, are assigned to the edges (staggered grid). Consider a constant cell size Δs with nodes s_i, $i = 1, \ldots, m$, the integral averages

over the control cells $[s_{i-1/2}, s_{i+1/2}]$ are characterized with the index $_i$, yielding

$$\begin{aligned} &\mathrm{d}\mathbf{r}_i = \mathbf{v}_i\,\mathrm{d}t, \qquad \|\Delta_s \mathbf{r}_{i+1/2}\| = 1, \\ &(\rho \mathrm{A})\,\mathrm{d}\mathbf{v}_i = \left(\Delta s^{-1}(\boldsymbol{\phi}_{i+1/2} - \boldsymbol{\phi}_{i-1/2}) + \mathbf{f}_i\right)\mathrm{d}t + \Delta s^{-1/2}\mathbf{A}_i \cdot \mathrm{d}\boldsymbol{w}_t \end{aligned}$$

with flux approximation

$$\boldsymbol{\phi}_{i+1/2} = N_{i+1/2}\Delta_s \mathbf{r}_{i+1/2} - \Delta_s\big((\mathrm{EI})\Delta_{ss}\mathbf{r}\big)_{i+1/2}.$$

The function values at $s_{i+1/2} = s_i + \Delta s/2$ are indicated with the index $_{i+1/2}$. The occurring derivatives are approximated with first order finite difference stencils, for example, $\Delta_s \mathbf{r}_{i+1/2} = (\mathbf{r}_{i+1} - \mathbf{r}_i)/\Delta s$. So, the discretized fiber becomes a polygon line with a fixed geometrical spacing for the spatial points associated with the nodes. The aerodynamic force terms are evaluated as $\mathbf{f}_i = (\mathbf{f}_{i-1/2} + \mathbf{f}_{i+1/2})/2$ (analogously for $\mathbf{A}_i$), this has the advantage that the tangents are only needed on the edges; fiber curve and velocity are averaged across the neighboring nodes. The necessary flow data is interpolated at the associated positions. The stochastic differential algebraic system with time-dependent Wiener process $\boldsymbol{w}$ is temporally treated with an implicit Euler-Maruyama method. Although the aerodynamic forces $\mathbf{f}_i$ in the core (in the fiber tangent and velocity) are implicitly incorporated, the flow data that appears in them is queried with the fiber position of the old time level, such that the resulting large nonlinear equation system can be solved using a Newton method with analytical Jacobi matrix and Armijo step-size control. The corresponding linear systems are treated with a band solver. The method is so well optimized with regard to assembling the Jacobian that the main effort per time step is due to the linear equation solver itself. For existence and convergence results we refer to [31].

For the nonholonomic contact constraints a Lagrange parameter λ_i and a Boolean variable $\delta_i \in \{0, 1\}$ are assigned algorithmically to each node s_i. The last characterizes the fiber movement type as either non-contacting (free) ($\delta_i = 0$) or contacting ($\delta_i = 1$),

$$(\rho \mathrm{A})\,\mathrm{d}\mathbf{v}_i = \cdots + \delta_i \lambda_i \frac{\nabla h_i}{\|\nabla h_i\|}\,\mathrm{d}t \quad \text{and} \quad \begin{cases} \lambda_i = 0, & \text{if } \delta_i = 0, \\ h_i = 0, & \text{if } \delta_i = 1. \end{cases}$$

The equations are solved in dependence on δ_i for each time step t^n to t^{n+1}. Although the Lagrange multipliers are distributions, this creates no problems for a finite Euler step. If, at the end of the time step, the condition $h(\mathbf{r}_i, t^{n+1}) > 0$ for free nodes or $\lambda_i > 0$ for contacting nodes is violated, the Boolean variable is switched to the other value and the entire time step is repeated for all nodes. This procedure is iterated until all fiber points move consistently. The required smoothness of the distance function h is essential for the performance of the Newton method. In practice, geometries in CFD simulations are described as triangular meshes implying $h(\cdot, t) \in C^0$. It is smoothed via a linear combination of the triangle plane distance functions that are weighted by radial Gaussian kernels normalized to give a partition of unity. For a new smoothing procedure based on convolutions see [32].

2.2 Aerodynamic web forming zone

The fiber suspension flow in the aerodynamic web forming zone is dilute. Therefore, we neglect fiber-fiber interactions as well as the fibers' impact on the air flow. The fibers leave

the rotating card cylinder continuously over time according to the machine's mass rate (Figure 2). Due to their inertia they collide with the baffle pipe before they are suctioned onto the conveyor belt by the downwards directed turbulent air flow. The turbulent flow fluctuations cause the fibers to swirl and to form a random web. We are interested in the fibers' distribution on the conveyor belt and their characteristic geometrical lay-down properties as starting point for generating the resulting nonwoven material by means of a stochastic surrogate lay-down model. Since the airlay process parameters are constant over time and all characteristic (statistic) properties are homogeneous in CD - apart from negligible boundary effects due to the plant edges - we can use the invariances when determining the transition probability of the process.

Consider the fixed Cartesian coordinate system $\{\mathbf{e_x}, \mathbf{e_y}, \mathbf{e_z}\}$ of the machinery, whose origin is located in the middle of the conveyor belt below the fiber dropping (cf. Section 1.1). Let $p : \mathbb{R}^5 \to \mathbb{R}$ be the transition probability that relates the fibers' dropping distribution density φ along the card cylinder and their deposition distribution density ψ on the conveyor belt over time, i.e.,

$$\psi(x, y, t) = \int_{\mathbb{R}^2} p(x, y, t; \check{y}, \check{t})\varphi(\check{y}, \check{t})\, \mathrm{d}\check{y}\, \mathrm{d}\check{t}.$$

Here, each fiber is represented by a single fiber point. Because of the process invariances in CD and time we have

$$p(x, y, t; \check{y}, \check{t}) = p(x, y - \check{y}, t - \check{t}; 0, 0) =: p_0(x, y - \check{y}, t - \check{t}).$$

We assume a maximal throwing range and a maximal lay-down time, hence there exist $y_{\max} > 0$ and $t_{\max} > t_{\min} > 0$ such that

$$p_0(x, y, t) = 0 \quad \text{for } |y| > y_{\max}, t \notin [t_{\min}, t_{\max}].$$

In the airlay process the fibers' dropping is equally distributed along the card cylinder with release width w and over the production time T, i.e., $\varphi(y, t) = 1_{[-w/2, w/2]}(y)1_{[0,T]}(t)/(wT)$ in terms of characteristic functions. This yields a deposition distribution density that is independent of y and t in the so-called region of homogeneity $\mathcal{H}$. The existence of this region, $\mathcal{H} \neq \emptyset$, is crucial for the production of a homogeneous nonwoven and can be ensured by adequate process settings. We get

$$\psi(x, y, t) = \frac{1}{wT} g(x), \quad g(x) = \int_{t_{\min}}^{t_{\max}} \int_{-y_{\max}}^{y_{\max}} p_0\left(x, y', t'\right) \mathrm{d}y'\, \mathrm{d}t' \tag{2.2a}$$

$$\text{in } \mathcal{H} = \left\{ (y, t) \;\middle|\; y \in \left(-\frac{w}{2} + y_{\max}, \frac{w}{2} - y_{\max} \right), t \in (t_{\max}, T + t_{\min}) \right\}. \tag{2.2b}$$

Especially $\int_{\mathbb{R}} g(x)\, \mathrm{d}x = 1$ is satisfied. We refer to g as probability density function for the lay-down MD positions. In the simulation we obtain the transition probability directly from the computed deposition density when using a Dirac-distributed dropping,

$$p_0(x, y, t) = \psi(x, y, t), \quad \text{if } \varphi(y, t) = \delta_0(y)\delta_0(t).$$

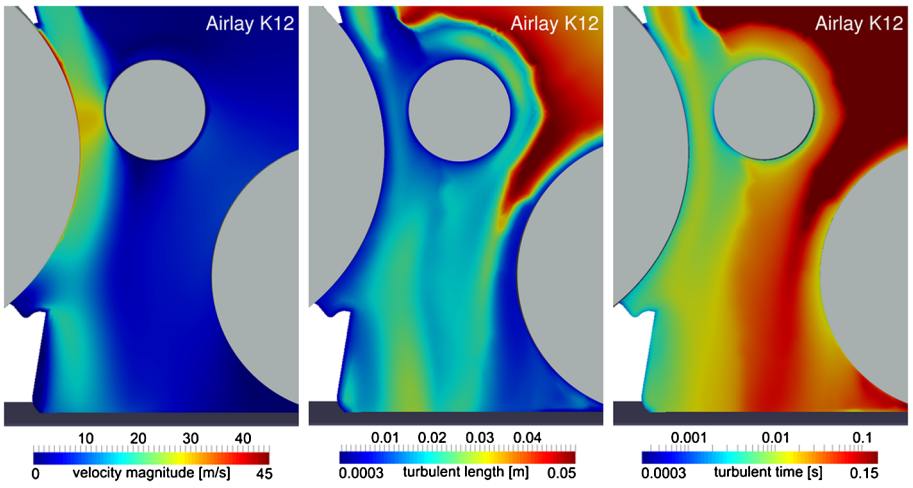

Figure 3 Turbulent flow field in the airlay process. *From left to right*: Mean velocity magnitude $\|\mathbf{u}\|$, turbulent length $l_T = k^{3/2}/\epsilon$ and turbulent time $t_T = k/\epsilon$. The plant geometry is colored in grey.

Coming to the actual process simulation: in the proposed one-way coupling we perform a stationary two-dimensional computation of the unloaded flow (MD cut plane), where the conveyor belt is realized as porous medium using Darcy's law. The flow quantities for the reference scenario are visualized in Figure 3. In addition to the mean velocity magnitude $\|\mathbf{u}\|$, we particularly show the turbulent length $l_T = k^{3/2}/\epsilon$ and time scales $t_T = k/\epsilon$ to give an impression of the occurring turbulent flow fluctuations with kinetic energy k and dissipation rate ϵ. To obtain a representative deposition behavior of the two different fiber types used in the airlay process, we compute the turbulence-driven three-dimensional dynamics of n_1 bicomponent and n_2 solid fibers, $n_1 = n_2 \gg 1$, based on (2.1a)-(2.1c). For the respective fiber material see Table 2. Each fiber enters the flow domain from the release center at time $t = 0$ as straight stress-free body that is oriented tangentially to the machine geometry and has the effective speed of the card cylinder. The fiber ends are treated as stress-free over time, i.e., $\partial_{ss}\mathbf{r}(s,t) = \partial_{sss}\mathbf{r}(s,t) = \mathbf{0}$, $N(s,t) = 0$ for $s \in \{0, \ell\}$, $t \geq 0$, until the fiber reaches the conveyor belt. To account for the deposition of many fibers within a short time period we realize the laying down by a modification of the boundary conditions instead of using Coulomb friction: as soon as the fiber comes in contact with the conveyor belt, the fiber point is fixed and transported with the belt speed. Note that the fiber raw material in the airlay process has a crimp on microscale which might affect the properties of the resulting microstructure. We realize the crimp in the surrogate lay-down model in Section 3, but it is not handled in the present Cosserat description for reasons of complexity. To ensure a consistent model chain with respect to mass conservation, we treat here the fibers with their crimped length ℓ and a respectively increased titer. Figure 4 shows the different dynamic behavior of the bicomponent and solid fibers. The heavier solid fibers collide earlier with the baffle pipe which is installed to avoid demixing. The solid fibers are less affected by the turbulent flow. Their deposition range is smaller, more pronounced and further away from the card cylinder. In contrast, the dynamics of the lighter bicomponent fibers is more diffused. The lay-down distributions of the two fiber types on the conveyor belt are presented in Figure 5. The figure particularly shows the distribution for the MD position of the fiber point that entered the flow domain at first in time, the distribution function

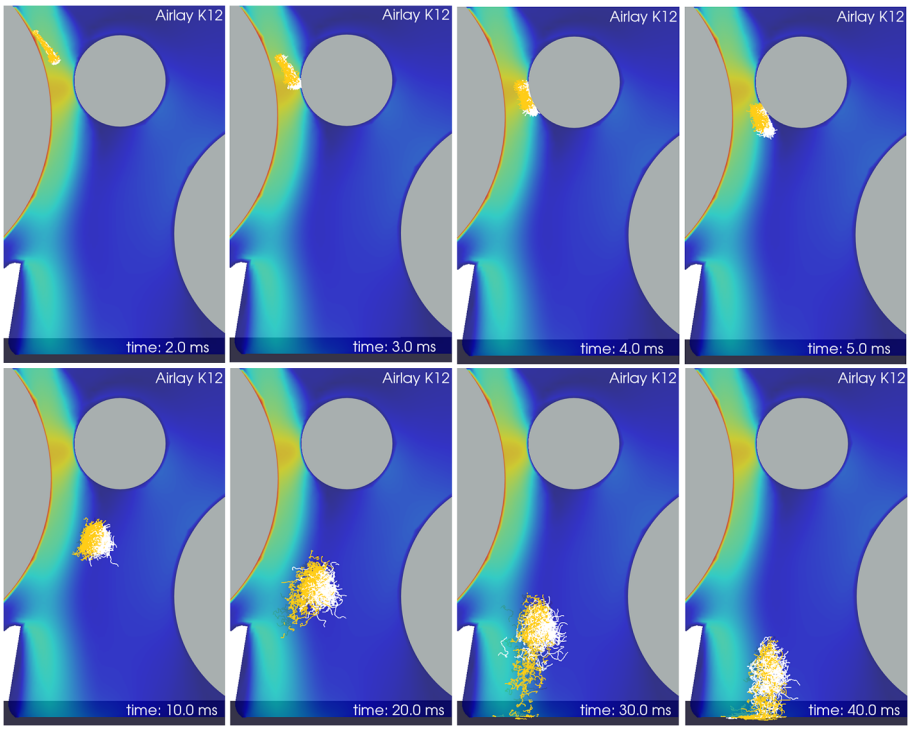

Figure 4 Typical fiber dynamics. Visualization of 100 bicomponent fibers (orange) and 100 solid fibers (white) that enter simultaneously the aerodynamic web forming zone and move over time. In the background the air flow is colored with the velocity magnitude, cf. Figure 3.

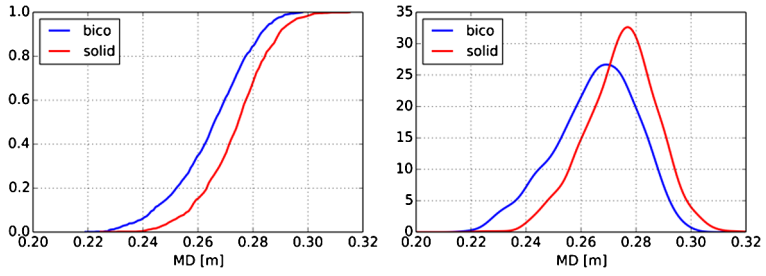

Figure 5 Fiber lay-down distribution. Probability distribution function G (*left*) and density g (*right*) of the lay-down MD position for the two fiber types (cf. (2.2a)), $G(x) = \int_{-\infty}^{x} g(x')\,\mathrm{d}x'$. The MD position is given in the fixed coordinate system of the machinery, it indicates the distance to the card cylinder.

is approximated by the superposition of the point measures, $g_j(x) \approx \sum_{k=1}^{n} \delta_{X_j^k}(x)/n$ with Dirac distribution δ, lay-down MD positions X_j^k associated to the fiber type $j = 1, 2$ and $n = 1{,}000$, cf. (2.2a). Note that the influence of the chosen referential fiber point on the probability density function is marginal in comparison to the applied smoothing on the discrete simulation data. The smoothing is performed with a kernel density estimation where the kernel's bandwidth is selected with respect to Scott's rule [33]. The mass rate of the machine and the conveyor belt speed have no effect on the fibers' deposition probability distribution, but they certainly affect the height of the resulting nonwoven material as we will discuss in Section 3.

3 Virtual microstructure generation

The produced nonwoven consists of millions of fibers. We are interested in its material properties that are determined by the microstructure (Figure 6). Since the described simulations of single elastic fibers in the turbulent air flow are computationally expensive and very time-demanding due to the huge amount of physical details, we introduce a surrogate model for the efficient virtual three-dimensional web generation. We describe the random topology of the microstructure by help of a stochastic lay-down model in the spirit of [11, 34], whose parameters are calibrated using a representative process simulation (cf. Section 2.2) and computer tomography data. On top of it we model the fiber associated material properties with an elastic Cosserat network. This network provides the basis for our virtual material investigations in Section 4. For modeling elastic multi-link structures we refer to [35], see also [14, 36, 37].

3.1 Random fiber web topology

The nonwoven is the deposition image of the fibers. A striking characteristic in the microstructure is a ramp-like contour surface, see Figure 6 for a photo of a nonwoven sample. After the aerodynamic web forming the nonwoven material is thermobonded in a post-processing step. As result of heating the bicomponent fibers melt and glue the random individual fibers together to a solid fiber network which is then explored in material testing. Our strategy is to use the contour surface that results from the lay-down probability densities as basis for stochastic modeling the three-dimensional deposition image with crimped fibers. We identify the contact points of the fibers in the random web, specify the adhesive joints and generate the net topology by help of a graph where the adhesive joints are interpreted as nodes and the fibers as edges. The resulting network is equipped with constitutive relations in Section 3.2.

We describe the contour line of the fiber material on the conveyor belt in MD by the graph of $R : \mathbb{R} \to [0, \mathrm{H}]$,

$$R(x) = \mathrm{H} \int_{-\infty}^{x} r\big(x'\big)\,\mathrm{d}x', \quad \text{with } r(x) = \beta_{n,1} g_1(x) + \beta_{n,2} g_2(x), \beta_{n,1} + \beta_{n,2} = 1, \tag{3.1}$$

where $\mathrm{H} > 0$ denotes the height of the nonwoven and r is the joined probability density of the deposited material, $\mathrm{supp}(r) = [x_{\min}, x_{\max}]$. In particular, g_1 and g_2 are the MD lay-down density functions of the two different fiber types that are obtained from the process

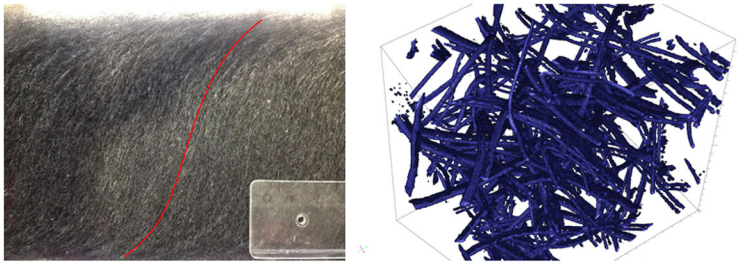

Figure 6 Nonwoven material sample after thermobonding. *Left*: Photo (MD cut plane), ramp-like contour line in microstructure. *Right*: Computer tomography scan of a sample section, visualization by Fraunhofer ITWM, Department Image Processing.

simulation (cf. Figure 5 and (2.2a)). The weights $\beta_{n,j}$ can be determined either with respect to the number ratio or the mass ratio of the fiber types. As we have a geometrical surrogate in mind, we use the number ratio that can be expressed by means of the known mass ratio $\beta_{m,1}/\beta_{m,2}$, the fiber titers and lengths (Table 2), so

$$\beta_{n,j} = \frac{\beta_{m,j}(\rho \mathrm{A})_i \mathrm{L}_i}{\beta_{m,1}(\rho \mathrm{A})_2 \mathrm{L}_2 + \beta_{m,2}(\rho \mathrm{A})_1 \mathrm{L}_1}, \quad j \neq i, j = 1, 2.$$

Since the nonwoven is homogeneous in CD in $\mathcal{H}$ (2.2b), the contour line R implies a contour surface in the microstructure (Figure 6).

Aiming for the three-dimensional nonwoven microstructure to investigate the material properties, we consider a cubic sample volume $\mathcal{V}$ over the nonwoven height H with base area d^2 that is associated to the homogeneity region $\mathcal{H}$. As any fiber that can be partially contained in $\mathcal{V}$ lies in $\mathcal{V}_\mathrm{R}$, i.e., $\mathcal{V} = [-d/2, d/2]^2 \times [0, \mathrm{H}] \subset [-d_\mathrm{R}/2, d_\mathrm{R}/2]^2 \times [0, \mathrm{H}] = \mathcal{V}_\mathrm{R}$ with $d_\mathrm{R} = d + 2L$, $L = \max_j \mathrm{L}_j$, we particularly deal with the reference sample $\mathcal{V}_\mathrm{R}$ with the extended base to avoid boundary effects. The microstructure is formed by the fibers' falling onto the conveyor belt according to the contour surface (graph of R) and the process mass rate $\dot{\mathrm{m}}$, while the belt moves with speed v_B. To account for the belt motion we introduce $x_\mathrm{B} : [0, T_\mathrm{R}] \to \mathbb{R}$,

$$x_\mathrm{B}(t) = x_{\min} - \frac{d_\mathrm{R}}{2} + \mathrm{v}_\mathrm{B} t, \qquad T_\mathrm{R} = \frac{1}{\mathrm{v}_\mathrm{B}}(x_{\max} - x_{\min} + d_\mathrm{R}),$$

where T_R is the time needed to produce a nonwoven of the reference size. The total number of fibers deposited uniformly in this time is given by

$$n_j = \beta_{m,j} \frac{\dot{\mathrm{m}}}{(\rho \mathrm{A})_j \mathrm{L}_j} \frac{d_\mathrm{R}}{\mathrm{b}} T_\mathrm{R}$$

for each type $j = 1, 2$ with the mass associated weights $\beta_{m,j}$. The ratio d_R/b with belt width b ensures the correct scaling in CD. Certainly, not all these fibers need to contribute to the reference sample $\mathcal{V}_\mathrm{R}$ because of the randomly distributed lay-down MD positions. In the following the index distinguishing the different fiber types is suppressed when not explicitly needed. We identify a deposited fiber with the lay-down time t and MD-CD-coordinates (X, Y) of its end point, i.e., (X, Y, t) with X being g_j-distributed, Y uniformly distributed in $[-d_\mathrm{R}/2, d_\mathrm{R}/2]$ and $t \in [0, T_\mathrm{R}]$. If especially $X - x_\mathrm{B}(t) \in [-d_\mathrm{R}/2, d_\mathrm{R}/2]$ is satisfied, the deposited fiber contributes to the sample $\mathcal{V}_\mathrm{R}$. We model the fiber in the three-dimensional web as stochastic process in terms of the curve (e.g., its centerline) $\boldsymbol{\eta}^{(X,Y,t)} : \mathcal{I} \to \mathcal{V}_\mathrm{R}$,

$$\boldsymbol{\eta}_s^{(X,Y,t)} = \mathbf{R}(X) \cdot \boldsymbol{\xi}_s + \big(X - x_\mathrm{B}(t)\big)\mathbf{e_x} + Y\mathbf{e_y} + R(X)\mathbf{e_z} \tag{3.2a}$$

$$\text{with } \mathbf{R}(X) = \frac{1}{\sqrt{1 + R'(X)^2}}\Big(\mathbf{I} + \big(\sqrt{1 + R'(X)^2} - 1\big)\mathbf{e_y} \otimes \mathbf{e_y} + R'(X)(\mathbf{e_z} \otimes \mathbf{e_x} - \mathbf{e_x} \otimes \mathbf{e_z})\Big),$$

$\mathbf{R}(X) \in \mathrm{SO}(3)$, via the stochastic Stratonovich differential system [34]

$$\mathrm{d}\boldsymbol{\xi}_s = \boldsymbol{\tau}_s \, \mathrm{d}s, \tag{3.2b}$$

$$\mathrm{d}\boldsymbol{\tau}_s = -\frac{1}{B+1}\left(\boldsymbol{\Pi}_s(B)\cdot\nabla V(\boldsymbol{\xi}_s)\,\mathrm{d}s + A\,\boldsymbol{\Pi}_s(\sqrt{B})\circ\mathrm{d}\boldsymbol{w}_s\right) \tag{3.2c}$$
$$\text{with } \boldsymbol{\Pi}_s(P) = \boldsymbol{\nu}_{\mathbf{1},s}\otimes\boldsymbol{\nu}_{\mathbf{1},s} + P\boldsymbol{\nu}_{\mathbf{2},s}\otimes\boldsymbol{\nu}_{\mathbf{2},s}$$

with $\boldsymbol{\xi}_0 = \mathbf{0}$, $\boldsymbol{\tau}_0$ uniformly distributed in the unit circle spanned by $\mathbf{e_x}$ and $\mathbf{e_y}$ as well as with $\mathbf{I}$ unit tensor. By construction, a fiber end point lies on the contour surface and the main fiber orientation is aligned to it, since the tangential plane in the end point is spanned by $\mathbf{e_x} + R'(X)\mathbf{e_z}$ and $\mathbf{e_y}$. The underlying stochastic process $((\boldsymbol{\xi},\boldsymbol{\tau}) : \mathcal{I} \to \mathbb{R}^3 \times \mathbb{S}^2)$ with unit sphere $\mathbb{S}^2 \subset \mathbb{R}^3$ in (3.2b)-(3.2c) is known as a three-dimensional anisotropic lay-down model for fiber position and orientation around the MD-CD plane, [11, 34]. It presents the path of a deposited fiber as image of an arc-length parameterized curve that is influenced by various (airlay) process parameters. Modeling the fiber orientation (tangent) $\boldsymbol{\tau}$, the drift term with the potential V describes the typical coiling behavior of the fibers, i.e., $V(\boldsymbol{\xi}) = \boldsymbol{\xi}\cdot\mathbf{C}^{-1}\cdot\boldsymbol{\xi}/2$ with $\mathbf{C} = \mathrm{diag}(\sigma_x^2,\sigma_y^2,\sigma_z^2)$ regarding the machinery coordinates. In particular, $\sigma_x, \sigma_y \geq 0$ denote the standard deviations of the fiber throwing onto the conveyor belt in MD and CD, and $\sigma_z > 0$ assures a height constraint. Accounting for the fluctuations in the airlay process, the drift is superposed by a white noise with the vector-valued Wiener process $(\boldsymbol{w} : \mathcal{I} \to \mathbb{R}^3)$ and the scalar amplitude A. The parameter $B \in [0,1]$ indicates the anisotropic behavior with the special local orthonormal right-handed director triad $\{\boldsymbol{\tau},\boldsymbol{\nu_1},\boldsymbol{\nu_2}\}$ where $\boldsymbol{\nu_1} \in \mathrm{span}(\mathbf{e_x},\mathbf{e_y})$, i.e., isotropy for $B = 1$, asymptotic reduction to two-dimensional planar lay-down [6, 38] for $B = 0$.

On microscale the fibers are characterized by a crimp with crimp number $\mathrm{C} \in \mathbb{N}_0$ (bows per unit length, cf. Table 2). The crimp can be incorporated in the surrogate lay-down model by introducing a curve $\boldsymbol{\gamma}$ that describes the crimp structure and using $\tilde{\boldsymbol{\xi}}$ instead of $\boldsymbol{\xi}$ in (3.2a), e.g.,

$$\tilde{\boldsymbol{\xi}}_s = \int_0^s \mathbf{Q}_{\boldsymbol{\xi}}(s')\cdot\frac{\mathrm{d}\boldsymbol{\gamma}}{\mathrm{d}s}(s')\,\mathrm{d}s', \qquad \boldsymbol{\gamma}(s) = s\mathbf{e_x} + c\sin(\mathrm{C}\pi s)\mathbf{e_y}. \tag{3.3}$$

The matrix-valued function $\mathbf{Q}_{\boldsymbol{\xi}} : \mathcal{I} \to \mathrm{SO}(3)$ represents the local $\boldsymbol{\xi}$-associated triad $\{\boldsymbol{\tau},\boldsymbol{\nu_1},\boldsymbol{\nu_2}\}$ with respect to the fixed coordinate system $\{\mathbf{e_x},\mathbf{e_y},\mathbf{e_z}\}$ of the machinery. The parameter $c \geq 0$ is implicitly given by the fiber length,

$$\mathrm{L} = \int_0^\ell \left\|\frac{\mathrm{d}\boldsymbol{\gamma}}{\mathrm{d}s}(s)\right\|\mathrm{d}s = \int_0^\ell \sqrt{1 + c^2(\mathrm{C}\pi)^2\cos^2(\mathrm{C}\pi s)}\,\mathrm{d}s.$$

Superposing bicomponent and solid fibers according to their MD lay-down distributions, number ratio and calibrated model parameters results in a virtual fiber web. To obtain the thermobonded nonwoven to $\mathcal{V}_\mathrm{R}$, the adhesive joints in the web are detected by help of a contact threshold $a \geq 0$ and the net topology is set up in terms of a graph. Details to the strategies and algorithms are given in the following subsections.

Parameter estimation and simulation. The parameters of the surrogate model (3.2a)-(3.2c) are calibrated to the airlay process, following the procedure for endless spunbond fibers in [3, 11]. Whereas A_j, $\sigma_{x,j}$, $\sigma_{y,j}$ and $\sigma_{z,j}$ depend on the specific fiber type ($j = 1,2$ for bicomponent and solid, respectively) and are estimated from a representative sample of dynamical fiber-flow simulations (cf. Section 2.2), the isotropy parameter B characterizes the total nonwoven produced. The required additional information about the full spatial

orientation is taken from computer tomography data (cf. Figure 6). The respective image processing and analysis were performed and provided by the Fraunhofer ITWM, Department Image Processing with the software[c] MAVI.

Consider the discretized fiber data of a dynamical process simulation after deposition on the MD-CD plane, i.e., $\mathbf{d}_i^k = (\mathbf{r}_i^k, \alpha_i^k)$ with fixed cell size Δs and orientation angle $\alpha_i^k \angle(\mathbf{e_x}, \partial_s \mathbf{r}_i^k)$, $i = 1, \dots, m$ for each fiber $k = 1, \dots, n$ corresponding to the same type, $\boldsymbol{d} = (\mathbf{d}_i^k)$. The noise amplitude A is related to the change of orientation in the MD-CD plane. For endless fibers the throwing range σ_x, σ_y is given by the stationary deposition distribution, cf. ergodicity theorem in [9]. Using the sample of process simulations (Section 2.2), we identify the parameters $\mathbf{p} = (A, \sigma_x, \sigma_y)$ as

$$\mathbf{p} = \boldsymbol{f}(\boldsymbol{d}),$$

$$\boldsymbol{f}(\boldsymbol{d}) = \left(\max_{h \in \mathbb{N}} \sqrt{\sum_{k=1}^{n} \sum_{i=1}^{m-h} \frac{(\alpha_{i+h}^k - \alpha_i^k)^2}{n(m-h)h\Delta s}}, \right.$$
$$\left. \sqrt{\sum_{k=1}^{n} \frac{((\mathbf{r}_1^k - \mathbf{r}_m^k) \cdot \mathbf{e_x})^2}{n}}, \sqrt{\sum_{k=1}^{n} \frac{((\mathbf{r}_1^k - \mathbf{r}_m^k) \cdot \mathbf{e_y})^2}{n}} \right).$$

The finite length of the staple fibers might affect the result if $\ell \not\gg \sigma$. In that case we estimate the parameters by the best approximation

$$\mathbf{p}^\star = \operatorname*{argmin}_{\mathbf{p} \in (\mathbb{R}_0^+)^3} \left\| \boldsymbol{f}\left(\boldsymbol{d}_{\mathrm{sur}}(\mathbf{p})\right) - \boldsymbol{f}(\boldsymbol{d}) \right\|^2,$$

where $\boldsymbol{d}_{\mathrm{sur}}(\mathbf{p})$ denotes the corresponding fiber data of the surrogate model (3.2b)-(3.2c). To solve the minimization problem, we apply a relaxated quasi Newton method with unit Jacobian and initial guess $\mathbf{p} = \boldsymbol{f}(\boldsymbol{d})$ [3].

Let θ be the angle of the fiber tangent out off the main plane. Its stationary distribution in the lay-down model (3.2b)-(3.2c) depends on the isotropy parameter B, i.e., $\rho_B(\theta) = c_B(\sin\theta)^{1/B}$ with normalization constant c_B. Using a data sample $\boldsymbol{\theta} = (\theta_1, \dots, \theta_r)$ provided from a computer tomography scan of a material section, we determine B by help of a maximum likelihood estimator

$$B^\star = \operatorname*{argmax}_{B \in (0,1]} \log f(B|\boldsymbol{\theta}), \quad f(B|\boldsymbol{\theta}) = \prod_{k=1}^{r} c_B(\sin\theta_k)^{1/B}.$$

The information about σ_z should be also concluded from the computer tomography scan in future. However, so far, the image analysis yields no reasonable results, such that we approximate here $\sigma_z = 0.1\sigma_y$.

Figure 7 shows the fiber deposition image associated to the reference scenario. The simulation of the stochastic lay-down model (3.2a)-(3.2c) is performed with an explicit Euler-Maruyama scheme with constant grid size $\Delta s = 10^{-4}$ [s] and an underlying lay-down time resolution of $\Delta t = 10^{-2}$ [m]. The calibrated model parameters are particularly $\mathbf{p}_1 = (0.289, 1.73 \cdot 10^{-2}, 1.83 \cdot 10^{-2})$ for the bicomponent fibers and $\mathbf{p}_2 = (0.238, 1.41 \cdot 10^{-2}, 1.99 \cdot 10^{-2})$ for the solid fibers, $B = 0.288$. The quantities are given in SI-units (A [$\mathrm{m}^{-1/2}$], σ [m], B [1]).

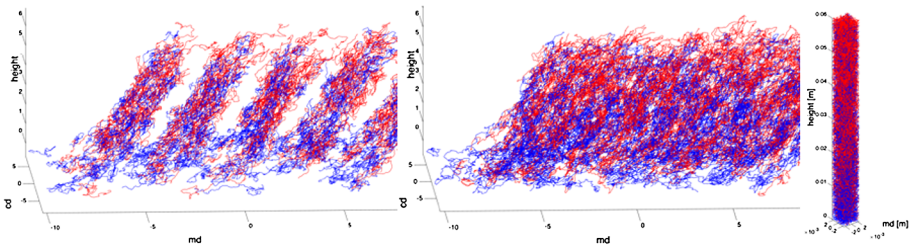

Figure 7 Virtual deposition image. Virtual deposition image with contour surface according to MD lay-down distributions (3.1) and calibrated surrogate fiber models (3.2a)-(3.2c). *Left and middle*: The numbers of bicomponent fibers (blue) and solid fibers (red) are scaled down for visualization issues. Axes units in $[10^{-2}$ m]. *Right*: Reference sample $\mathcal{V}_{\mathrm{R}}$.

Detection of adhesive joints. The microstructure of the thermobonded nonwoven is the random web of the deposited fibers that is glued together by the bicomponent fibers. In terms of graph theory the random net topology can be represented by a graph $\mathcal{G} = (\mathcal{N}, \mathcal{E})$ where the adhesive joints are considered as the nodes and the fiber curves as the edges. Here, $\mathcal{N}$ and $\mathcal{E}$ denote the index sets of nodes and edges, respectively.

For the identification of adhesive joints in the web (Figure 7, right), we restrict on the fiber points that are associated to the spatial discretization of the individual fibers (in the lay-down model) as possible contact points. With m points per fiber $\boldsymbol{\eta}$ and n fibers in total, comparing all data points with another has the complexity $\mathcal{O}((mn)^2)$. As we deal with plenty of fibers, a direct pointwise comparison would be by far computationally too expensive. The bounding box method that is well-known from computer graphics meets our demands on efficiency. For details and more sophisticated methods we refer to [39, 40] and references therein. We embed each fiber in a box aligned to the coordinate axes and check pairwise if the boxes intersect or not. If the intersection is empty, there are obviously no contact points. Otherwise, we restrict on the fiber parts in the intersection box and iterate the procedure. Finally, two cases can occur: either the intersection of the bounding boxes keeps unchanged or the number of fiber points in the intersection is sufficiently small. In both cases the naive pairwise computation of distances between the sets of fiber points $\mathcal{F}$ and $\widehat{\mathcal{F}}$ belonging to two different fibers is used to detect possible contact points,

$$\left(\mathbf{x}^\star, \hat{\mathbf{x}}^\star\right) = \operatorname*{argmin}_{(\mathbf{x},\hat{\mathbf{x}})\in\mathcal{F}\times\widehat{\mathcal{F}}} \|\mathbf{x} - \hat{\mathbf{x}}\|.$$

In general, this minimizer is not unique. We take the first minimizer found for practical reasons. Two fibers are considered to be in contact in the point $\mathbf{a}$, if

$$\left\|\mathbf{x}^\star - \hat{\mathbf{x}}^\star\right\| \le a, \qquad \mathbf{a} = \frac{1}{2}\left(\mathbf{x}^\star + \hat{\mathbf{x}}^\star\right), \tag{3.4}$$

where the contact threshold $a \ge 0$ has to be chosen appropriately (see Section 4). In case that a bicomponent fiber is involved in the contact, we refer to $\mathbf{a}$ as adhesive joint and replace $\mathbf{x}^\star$ in $\mathcal{F}$ and $\hat{\mathbf{x}}^\star$ in $\widehat{\mathcal{F}}$ by $\mathbf{a}$. The adhesive joints - together with the fibers' end points - act as nodes in the resulting fiber network. Figure 8 shows the fiber net topology that corresponds to a section of the virtual deposition image $\mathcal{V}_{\mathrm{R}}$ in Figure 7(right) before and after contact detection. Alternatively, the resulting fiber graph could be also refined by

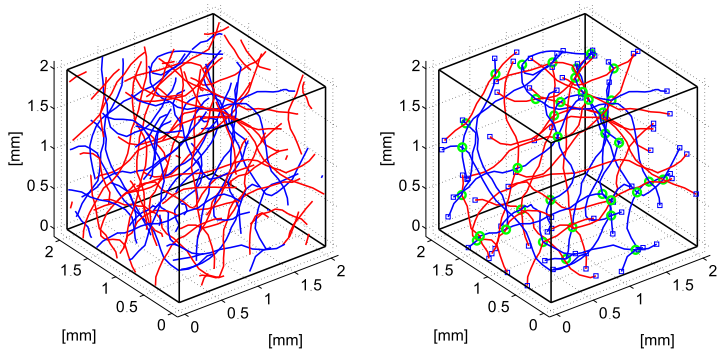

Figure 8 Fiber net topology. Net topology before (*left*) and after (*right*) contact detection for a section of $\mathcal{V}_R$ (cf. Figure 7, right), $a = 10^{-5}$ [m]. Disconnected fibers are deleted. Bicomponent fibers are colored in blue, solid fibers in red. The adhesive joints are marked by the green circles, the fibers' end points by the squares.

treating the set of all fiber discretization points as nodes. Disconnected subgraphs might be deleted from the network.

3.2 Elastic fiber net

For the subsequent material investigations we equip the fiber network with constitutive relations. An edge of the graph $\mathcal{G} = (\mathcal{N}, \mathcal{E})$ is associated with a fiber piece. Due to its slender geometry angular momentum effects are negligibly small such that we model it as a truss. A truss network in a stress-free reference configuration is described by the set of fiber node points $\{\mathbf{r}^{0\nu} \in \mathbb{R}^3, \nu \in \mathcal{N}\}$ and fiber edges $\mathbf{r}^{\mathbf{0}}_{\mu} \in \mathbb{P}_1([0, L_\mu], \mathbb{R}^3)$, $\|\mathrm{d}\mathbf{r}^{\mathbf{0}}_{\mu}/\mathrm{d}s\| = 1$, $\mu \in \mathcal{E}$ which are related according to $\mathbf{r}^{0\nu_p} \in \{\mathbf{r}^{\mathbf{0}}_{\mu_p}(0), \mathbf{r}^{\mathbf{0}}_{\mu_p}(L_\mu)\}$ for all $\mu_p \in \mathcal{E}(\nu_p)$. Here, $\mathcal{E}(\nu)$ denotes the index set of edges connected to the node ν, and $\mathbb{P}_1$ the set of linear polynoms. The actual position $\mathbf{r}^\nu$, $\mathbf{r}_\mu$ and inner forces $\mathbf{n}_\mu$ of the truss network are determined by the system of differential algebraic equations

$$\frac{\mathrm{d}\mathbf{r}_\mu}{\mathrm{d}s} = \mathbf{t}_\mu, \qquad \frac{\mathrm{d}\mathbf{n}_\mu}{\mathrm{d}s} = \alpha\left(\mathbf{r}_\mu - \mathbf{r}^{\mathbf{0}}_{\mu}\right), \quad \mathbf{n}_\mu = N(\varepsilon_\mu)\frac{\mathbf{t}_\mu}{\|\mathbf{t}_\mu\|}, \varepsilon_\mu = \|\mathbf{t}_\mu\| - 1, \tag{3.5a}$$

$$\sum_{\mu \in \mathcal{E}(\nu)} \mathbf{n}^\nu_\mu = \mathbf{0} \tag{3.5b}$$

for interior nodes $\nu \in \mathcal{N}_I$, supplemented with $\mathbf{r}^\nu = \hat{\mathbf{r}}^\nu$ (Dirichlet conditions) at fixed boundary nodes $\nu \in \mathcal{N}_{Bd}$ and $\mathbf{n}^\nu_\mu = \mathbf{0}$ (stress-free conditions) at free moving boundary nodes $\nu \in \mathcal{N}_{Bs}$, where $\mathcal{N} = \mathcal{N}_I \cup \mathcal{N}_{Bd} \cup \mathcal{N}_{Bs}$. The force balance (3.5b) is fulfilled at all nodes with $\mathbf{n}^\nu_\mu$ being the inner force of edge μ at node ν. Along a fiber edge the truss model only admits tangential forces. To incorporate the fiber crimp we use an effective elastic material law N for $\mathbf{n}_\mu$ that is nonlinear in the strains ε_μ and that we deduce from simulations of a respective beam model. Moreover, in contrast to a usual truss network model where $\mathrm{d}\mathbf{n}_\mu/\mathrm{d}s = \mathbf{0}$ holds, we regard the stiffness of the net due to the fibers' entanglement by means of the parameter $\alpha > 0$. Considering (3.5a)-(3.5b) in the context of energy minimization, the introduction of $\alpha \ll 1$ can be viewed as Tikhonov-type regularization of the corresponding minimization problem which ensures the uniqueness of the solution. For a study concerning the choice of α see Section 4. For the subsequent numerical tensile strength tests we discretize (3.5a)-(3.5b) with a node basis of linear shape functions (finite elements) and

employ a Newton-Raphson method for the resulting system of nonlinear equations. Note that - alternatively to the position - the displacement field $\mathbf{u} = \mathbf{r} - \mathbf{r^0}$ is often considered as unknown in literature, see, e.g., [37, 41].

Effective force modeling based on beam behavior. We deduce the effective force model N for a truss (3.5a) from energetic investigations of stress-strain relations for a geometrically exact beam subjected to axial displacements. In the special Cosserat rod theory [29] a beam is characterized by a curve (e.g., its centerline) $\mathbf{r} : [0, L] \to \mathbb{R}^3$ for the position and a rotational group $\mathbf{\Lambda} : [0, L] \to \mathrm{SO}(3)$ for the orientation of the planar cross-sections. Let $\{\mathbf{e_1}, \mathbf{e_2}, \mathbf{e_3}\}$ be a fixed outer orthonormal basis, then we consider a beam in the $\mathbf{e_1}$-$\mathbf{e_2}$ plane. The quantities associated with a stress-free reference configuration are indicated with the index $^\mathbf{0}$, in particular $(\mathbf{r^0}(L) - \mathbf{r^0}(0)) = l\mathbf{e_1}$, $l \leq L$, $\mathbf{\Lambda^0} \cdot \mathbf{e_1} = \mathrm{d}\mathbf{r^0}/\mathrm{d}s = \mathbf{t^0}$ ($\|\mathbf{t^0}\| = 1$) and $\mathbf{\Lambda^0} \cdot \mathbf{e_3} \equiv \mathbf{e_3}$ are assumed. Hence, $\mathbf{r^0}$ is an arc-length parametrized curve of total length L with crimped length l. We model the beam deformations due to an axial displacement $u \in \mathbb{R}$ in $\mathbf{e_1}$ by

$$\frac{\mathrm{d}\mathbf{r}}{\mathrm{d}s} = \mathbf{t}, \qquad \frac{\mathrm{d}\mathbf{\Lambda}}{\mathrm{d}s} = \boldsymbol{\kappa} \times \mathbf{\Lambda}, \qquad \frac{\mathrm{d}\mathbf{n}}{\mathrm{d}s} = \mathbf{0}, \qquad \frac{\mathrm{d}\mathbf{m}}{\mathrm{d}s} = \mathbf{n} \times \mathbf{t},$$
$$\mathbf{n} = \mathbf{\Lambda} \cdot \mathbf{C_n} \cdot \mathbf{\Lambda}^T \cdot \left(\mathbf{t} - \mathbf{t^0}\right), \qquad \mathbf{m} = \mathbf{\Lambda} \cdot \mathbf{C_m} \cdot \mathbf{\Lambda}^T \cdot \left(\boldsymbol{\kappa} - \boldsymbol{\kappa^0}\right),$$
$$\text{with } \left(\mathbf{r}(0), \mathbf{r}(L)\right) = \left(\mathbf{r^0}(0), \mathbf{r^0}(L) + u\mathbf{e_1}\right), \mathbf{\Lambda}(s) \cdot \mathbf{e_1} = \mathbf{t}/\|\mathbf{t}\|(s), \mathbf{\Lambda}(s) \cdot \mathbf{e_3} = \mathbf{e_3}, s \in \{0, L\}.$$

The material laws for inner forces $\mathbf{n}$ and torques $\mathbf{m}$ are linear in tangent $\mathbf{t}$ and curvature $\boldsymbol{\kappa}$, where $\mathbf{C_n} = (\mathrm{GA})\mathbf{P}_{\mathrm{E/G}}$ and $\mathbf{C_m} = (\mathrm{EI})\mathbf{P}_{\mathrm{2G/E}}$ with $\mathbf{P}_z = z\mathbf{e_1} \otimes \mathbf{e_1} + \mathbf{e_2} \otimes \mathbf{e_2} + \mathbf{e_3} \otimes \mathbf{e_3}$, $z \geq 0$, and the respective fiber properties E, G, A and I (cf. Table 2). For numerical details to beam simulations we refer to [37, 41]. Evaluating $\varepsilon = u/l$, $N = \mathbf{n}(L) \cdot \mathbf{e_1}$ for various $u \in \mathbb{R}$, the resulting stress-strain relation of the beam model is exemplified for two variants of crimped fibers (sinusoidal and zigzag crimp) in Figure 9. The relation involves an effective elastic material law $N(\varepsilon)$, $\varepsilon \in \mathbb{R}$ for the truss model in (3.5a).

Since the stress-strain relation reveals two characteristic regimes we think of an analytical surrogate that describes linearly fiber straightening for $0 \leq \varepsilon < \varepsilon^\star$ and fiber stretching

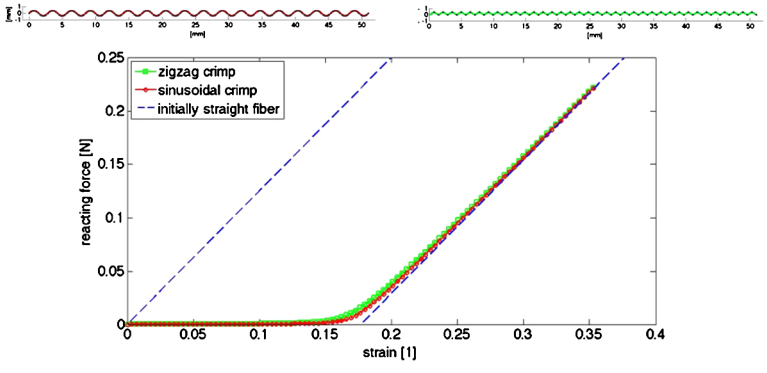

Figure 9 Stress-strain relation of beam model. Stress-strain relation for crimped fibers (sinusoidal and zigzag crimp) with $(L, l) = (\mathrm{L}, \ell)$ (cf. Table 2, solid), $\varepsilon^\star = 0.177$. Resulting effective force $N(\varepsilon)$, $\varepsilon \in \mathbb{R}$ for the truss (3.5a).

for $\varepsilon > \varepsilon^\star$ with $\varepsilon^\star = (L - l)/l$,

$$N(\varepsilon) = \begin{cases} N^\star/\varepsilon^\star \varepsilon, & 0 \le \varepsilon \le \varepsilon^\star, \\ N^\star + \mathrm{EA}/(1+\varepsilon^\star)(\varepsilon - \varepsilon^\star), & \varepsilon^\star < \varepsilon, \end{cases} \qquad N^\star = \mathrm{EI}/\big(l\varepsilon^\star\big) \int_0^L \big(k^0(s)\big)^2 \,\mathrm{d}s. \quad (3.6)$$

In the straightening phase stretching is assumed to be negligibly small such that $N^\star$ is the force exclusively required to pull out the underlying crimp. In (3.6) k^0 represents the geometrical curvature of the arc-length parametrized crimped initial curve $\mathbf{r^0}$, i.e., $(k^0)^2 = \|\mathrm{d}^2\mathbf{r^0}/\mathrm{d}s^2\|^2$. The integral $J_k = \int_0^L (k^0(s))^2 \,\mathrm{d}s$ depends obviously on the crimp structure, although the simulations indicate that the differences are small (cf. Figure 9). Analyzing the case of a sinusoidal crimp that has been proposed in (3.3), we proceed from the initial fiber curve $\tilde{\mathbf{r}}^{\mathbf{0}}(\tilde{s}) = \tilde{s}\mathbf{e_1} + c\sin(\mathrm{C}\pi\tilde{s})\mathbf{e_2}$, $\tilde{s} \in [0, l]$ with crimped length l, crimp number $\mathrm{C} \in \mathbb{N}_0$ (bows per unit length) and amplitude $c \ge 0$. Note that $\tilde{\mathbf{r}}^{\mathbf{0}}$ is not arc-length parametrized. Assuming $\delta = c\mathrm{C}\pi$ to be small and performing an asymptotic expansion in δ yields $J_k = 2(\mathrm{C}\pi)^2 l\varepsilon^\star + \mathcal{O}(\delta^4)$. Hence, $N^\star \approx 2(\mathrm{C}\pi)^2\mathrm{EI}$ holds. Changes in the crimp structure might affect the real factor occurring in the force term $N^\star$. For higher regularity the surrogate effective force model (3.6) can certainly be smoothed in $\varepsilon^\star$. Moreover, the introduction of a barrier function for negative strains might be reasonable to prevent the truss (3.5a) from degenerating to zero length at $\varepsilon = -1$.

4 Investigation of effective nonwoven material behavior

The quality of the produced nonwoven material is assessed by certain properties, among others, the tensile strength. An experimental tensile strength test on thermobonded nonwoven samples reveals the characteristic stress-strain relation for the material within the measurement accuracies (cf. Figure 10). Being interested in numerical material investigations we perform virtual tensile strength tests on basis of the microstructure generated in Section 3. For this purpose we further reduce the model complexity by applying homogenization techniques and effective material laws in the spirit of [36, 42]. In the virtual strength tests we particularly study the influence of the model parameters.

4.1 Virtual tensile strength test

In the one-dimensional experimental tensile strength test a cuboidal material sample over the full fabric height H is glued with the upper and lower faces onto two parallel plates.

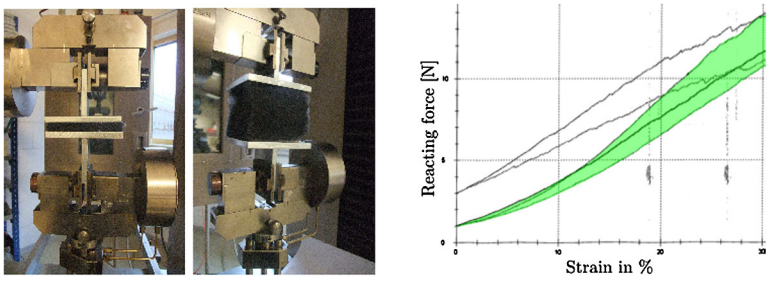

Figure 10 Tensile strength test for thermobonded nonwoven material samples. *Left*: Experimental set-up (test DIN-norm GME 60349). *Right*: Measured curves for stress-strain relation under the same experimental conditions. The green region indicates the reliability zone within the measurement accuracy for a pre-tensioning force F^0 and a sample size of base length/width w and fabric height H ($F^\circ = 1$ [N], $\mathrm{w} = 0.1$ [m], $\mathrm{H} = 0.06$ [m]). Photos, measurements and graphical evaluation by IDEAL Automotive.

The plates are pulled apart in direction of the nonwoven height while the reacting tensile force F is recorded as function of the strain ε. The strain is thereby determined from the actual sample height H as $\varepsilon = (H - H^\circ)/H^\circ$ with the referential height H° corresponding to a pre-tensioning force F°, see Figure 10.

The experimentally investigated sample $\mathcal{V}_\mathrm{E}$ is in general too huge for direct numerical simulations, e.g., in the considered industrial scenario the total length of contained fibers is approximately 10 km. Since the sample is taken from the homogeneity region of the airlay process, it is plausible to assume that its stochastic behavior is in average periodic in the base directions (being associated to MD and CD of the process). Thus, $\mathcal{V}_\mathrm{E}$ can be considered as assembly of n disjoint thin equal sample columns (cf. reference sample $\mathcal{V}_\mathrm{R}$, Section 3.1), and its tensile behavior can be concluded from exclusively investigating a single column $\mathcal{V}_\mathrm{R}$ and linearly superposing the result: the tensile force to $\mathcal{V}_\mathrm{E}$ equals n-times the tensile force to $\mathcal{V}_\mathrm{R}$ for given strain. To further reduce the model complexity for the virtual strength tests we approximate the column-like reference sample $\mathcal{V}_\mathrm{R}$ with the microstructure generated in Section 3 by an inhomogeneous truss model (see Figure 11). Therefore, we determine an effective material law by means of energetic homogenization using the Hill-Mandel-principle [36, 42]. In an inhomogeneous truss model the inner (tangential) force $N : [0, \mathrm{H}] \to \mathbb{R}$ arising from an applied tensile force f obeys

$$\frac{\mathrm{d}}{\mathrm{d}s} N\big(\varepsilon(s), s\big) = 0, \quad \text{with } N\big(\epsilon(\mathrm{H}), \mathrm{H}\big) = f.$$

Considering a partition of $[0, \mathrm{H}]$ into subintervals $I_i = [s_{i-1}, s_i)$, $i = 1, \dots, m$, with respect to an increasing sequence of nodes $\{s_i\}$ along the truss, $(s_0, s_m) = (0, \mathrm{H})$, we impose $N(\varepsilon(s), s) = N_i(\varepsilon(s))$ for $s \in I_i$. Assuming $\mathrm{d}N_i/\mathrm{d}\varepsilon \neq 0$, the strains are constant $\varepsilon(s) = \epsilon_i$ for $s \in I_i$. Hence,

$$N_i(\epsilon_i) = f \quad \text{in } I_i, \text{with } |I_i| = h_i, i = 1, \dots, m \tag{4.1}$$

holds according to the force balance. Regarding the sample column $\mathcal{V}_\mathrm{R}$, the truss intervals I_i are identified with representative volume elements (RVE) of height h_i that reflect the contour surface of the microstructure and the effective force models N_i are concluded from simulations of the elastic fiber net in the respective RVEs. In view of the tensile strength tests we restrict to $N_i : \mathbb{R}_0^+ \to \mathbb{R}_0^+$, presupposing $N_i(0) = 0$, $N_i(\epsilon) \to \infty$ as $\epsilon \to \infty$ and surjectivity. By this, the existence of solutions to (4.1) is ensured. If several solutions are possible, we consider the smallest strain. Consequently, the effective tensile behavior of the underlying huge material sample $\mathcal{V}_\mathrm{E}$ can then efficiently be computed for given force $F \in \mathbb{R}_0^+$ from the following effective strain and height functions $\varepsilon^{\mathrm{ef}}$, H^{ef},

$$\varepsilon^{\mathrm{ef}}(F) = \frac{H^{\mathrm{ef}}(F) - H^{\mathrm{ef}}(F^\circ)}{H^{\mathrm{ef}}(F^\circ)} \tag{4.2}$$

$$\text{with } H^{\mathrm{ef}}(F) = \sum_{i=1}^{m} h_i \varepsilon_i\left(\frac{F}{n}\right), \varepsilon_i(f) = \min\left\{\operatorname*{argmin}_{\epsilon \in \mathbb{R}_0^+} \big|N_i(\epsilon) - f\big|\right\}.$$

Effective force modeling based on fiber net behavior and RVE treatment. The effective force model N_i (4.1) is deduced from energetic investigations of the stress-strain relations for the ith RVE with the elastic fiber net (3.5a)-(3.5b) subjected to axial displacements - in analogy to the procedure presented in Section 3.2. Considering the RVE of referential

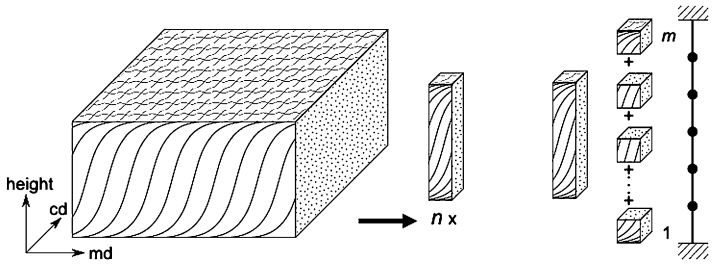

Figure 11 Reduction of sample complexity for virtual tensile strength tests. *From left to right*: sample $\mathcal{V}_E$ in experiment, column-like sample $\mathcal{V}_R$ of microstructure generation that is partitioned into a sequence of representative volume elements and approximated by an inhomogeneous truss model with effective material law.

Figure 12 Tensile strength simulation with RVE. RVE with fiber truss network for $\varepsilon = 0$ (*left*) and $\varepsilon = 0.6$ (*right*). Axes units in [10^{-3} m]. Trusses are colored with respect to inner forces: no forces in blue, increasing forces from dark/light green to deep red.

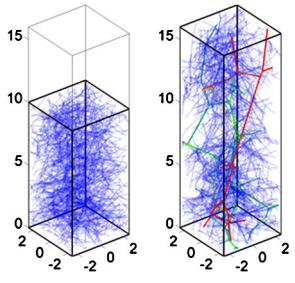

height h_i (Figure 11), all fiber node points at the upper face are vertically shifted with magnitude u, i.e., $\mathbf{r}^v = \mathbf{r}^{0v} + u\mathbf{e_z}$, $v \in \mathcal{N}_{B,up}$, while the ones at the lower face are kept at the referential positions. At the lateral faces only motions on the face plane are allowed. Evaluating $\varepsilon = u/h_i$, $N_i = \sum_{v\in\mathcal{N}_{B,up}} \sum_{\mu\in\mathcal{E}(v)} \mathbf{n}_\mu^v \cdot \mathbf{e_z}$ for various $u \in \mathbb{R}_0^+$ yields then the effective force function.

The partition and size of the RVEs are chosen with respect to two demands: the RVEs must show the characteristics of the microstructure (non-homogeneity over height, contour surface, fiber properties), while the computational effort for the simulation has to be practically manageable. In a RVE only connected subgraphs that contain fiber node points at both, the upper and the lower, faces contribute to the reacting force. Hence, without altering the tensile behavior, we delete all other components from the fiber network to reduce the degrees of freedom for the simulation. In addition free ends, i.e., nodes with multiplicity 1 at which no boundary conditions are imposed, have no impact and are deleted. Serial subgraphs, where elements are connected by nodes with multiplicity 2 at which no boundary conditions are imposed, might give rise to singularities in the numerics and may therefore be interpreted as a single edge with an adapted material law. For a visualization of a RVE under increasing tensile force we refer to Figure 12.

4.2 Stress-strain results

In the experimental tensile strength test with fixed sample size and pre-tensioning force the measured stress-strain curves for the thermobonded nonwoven material samples show a large volatility, in particular for increasing strains $\varepsilon > 0.2$. This observation is exemplified by three (measured) curves in Figure 13 that correspond to the reliability zone within the measurement accuracy (cf. Figure 10). The simulated stress-strain relations -

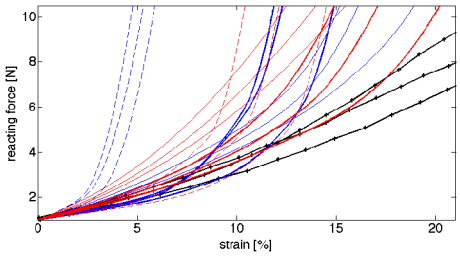

Figure 13 Stress-strain results for $\mathcal{V}_E$. Results provided by measurements (black lines, cf. green region in Figure 10) and by simulations for varying model parameters: RVE height h_i [10^{-3} m], net stiffness α [N/m^2] and contact threshold a [10^{-6} m]. Here: $h_i = 10, 15$ (blue, red lines); $\alpha = 10^{-6}, 10^{-5.5}, 10^{-5}$ (dashed, thick solid, thin solid lines); $a = 7.5, 7, 6.5$ (higher a implies steeper slope of curves).

that are computed on basis of our established process model chain - match the experimental ones in principle. But the simulation results are obviously affected by the model parameters for the fiber net, as variations of the topological contact threshold a (3.4), material stiffness α (3.5a)-(3.5b) and RVE height h_i for the vertical non-homogeneity (4.1) show, see Figure 13. As already discussed, the introduction of the parameter h_i is due to numerical reasons. Its choice has to ensure the representative character of the RVE and can be determined by several simulation runs. In the industrial scenario at hand, $h_i \approx 1.5 \cdot 10^{-2}$ [m] yields reasonable results by trend. Investigating the impact of the other two parameters, the study of the contact threshold a reveals a robust tensile behavior whereas changes of the net stiffness α are very sensitive. A larger contact threshold a causes an increasing number of adhesive joints and hence a more connected net topology. This implies a stiffer material behavior which is seen in slightly steeper stress-strain curves. However, this effect is mainly restricted to small strains, the further behavior (shape) of the curves is unchanged. In the airlay process the contact threshold of the net is related to the post-processing step of thermobonding. Depending on process parameters, such as adhesive properties of the used fiber material, temperature and duration of the thermobonding, the threshold a could be calibrated from experimental data. In contrast to a, the link between the model parameter α and the process parameters is not evident at all. From the mathematical point of view α is a relaxation parameter that ensures the uniqueness of the truss network solution. It might be interpreted in the context of net stiffness due to fibers' entanglement, but the explanation is vague. We observe that changing α strongly affects not only the slope but also the curvature of the stress-strain curves. Note that in a classical truss network model $\alpha = 0$ holds true. At this point of the simulation study, $\alpha \approx 10^{-5.5}$ [N/m^2] turns out to give an effective material behavior of the specific nonwoven sample which is comparable to the measurements. However, to get a general understanding of α in view of the airlay process parameters a sensitivity analysis in combination with a broader experimental study is necessary. At last, the simulated stress-strain curves indicate generally a stiffer material behavior for higher strains than the measured curves. The reason might be that the net topology, in particular the adhesive joints, is kept in the simulation - even under large tensile forces, whereas the fiber web rips and undergoes plastic changes in the experiment. This discrepancy might be overcome by introducing an additional parameter, a damage threshold, in the elastic net model. Its calibration requires certainly information about the nature of the adhesive joints and hence a deeper investigation of the post-processing step of thermobonding.

5 Conclusion and outlook

In this paper, we established a consistent, efficiently evaluable chain of mathematical models that enabled the simulation of the airlay process and the investigation of the resulting

material properties by virtual tensile strength tests. For the long-term industrial objective, the simulation-based process design towards the prediction and improvement of product properties, the mathematical mapping between the parameters of process and material is essential. We gave a proof of concept and showed the feasibility of a future optimization by applying our model chain to an industrial set-up. Proceeding from an airlay process simulation with a highly turbulent dilute fiber suspension flow, we used the process parameters (including fiber properties) and the numerically obtained deposition results to set up the stochastic surrogate model for the microstructure generation. Thereby, certain topological web parameters that characterize anisotropy, adhesive joints and height of the microstructure have to be identified from computer tomography data and calibrated by experiments (thermobonding effects). So far, the evaluation of the fiber distribution in height direction lacks from the image analysis of the computer tomography scans, but respective research work is in progress. The effective nonwoven material laws were deduced from the underlying fiber properties and simulation runs using energetic homogenization techniques. In the tensile strength tests the simulated and measured material behaviors match well for small strains but deviate for higher strains. This discrepancy might be due to plastic changes (rupture) that are not handled in the present elastic fiber net model. The break-up of adhesive joints could be certainly included but requires a deeper insight in the mechanism of thermobonding that was not analyzed in this paper.

At this point of research, however, we still face a difficulty: the model chain contains one parameter that was introduced for mathematical reasons, i.e., well-posedness of the elastic fiber net model, but turned out to strongly influence the tensile behavior. To gain understanding of its dependencies on the process parameters which will be necessary for future optimization issues, a sensitivity analysis in combination with a broader experimental study might be helpful.

Competing interests
The authors declare that they have no competing interests.

Authors' contributions
The process simulation comes from SG, RW and NM, the microstructure generation from CN and AK, the material investigations from CS and GL. NM and RW established the consistent model chain from process to material. NM wrote and all authors approved the final manuscript.

Author details
[1]Fraunhofer ITWM, Fraunhofer Platz 1, Kaiserslautern, 67663, Germany. [2]Fachbereich Mathematik, TU Kaiserslautern, Erwin-Schrödinger-Str. 48, Kaiserslautern, 67663, Germany. [3]Department Mathematik, FAU Erlangen-Nürnberg, Cauerstr. 11, Erlangen, 91058, Germany.

Authors' information
The research work that is presented in this article was developed in a joint project with groups from the University of Nürnberg-Erlangen and Kaiserslautern as well as from the Fraunhofer Institute for Industrial Mathematics, Kaiserslautern. The project addressed mathematics for innovations in the technical textile industry. Two companies were involved in the project, supporting the work with data and experience. Selected as a EU-MATHS-IN success story, the results were presented at the ECMI Conference 2016.

Acknowledgements
The authors thank their industrial partners, Dr. Joachim Binnig and Christopher Schütt from AUTEFA Solutions as well as Olaf Döhring from IDEAL Automotive, for performing measurements, providing data and information about process and fabric and supporting the work with fruitful discussions. Moreover, the financial support of the German Bundesministerium für Bildung und Forschung, Project OPAL 05M13, is acknowledged.

Endnotes
[a] www.ansys.com.
[b] www.itwm.fraunhofer.de. FIDYST is a software tool for fiber dynamics simulations, developed by the Fraunhofer ITWM, Germany. For details on the applicability spectrum, interfaces and algorithms we refer to [2]. We sketch here briefly the underlying relevant numerical schemes.

[c] www.mavi-3d.de. MAVI (Modular algorithms for volume images) is a Fraunhofer software for image processing, analysis and visualization, for details we refer to [43, 44].

Received: 1 September 2016 Accepted: 18 November 2016 Published online: 01 December 2016

References

1. Albrecht W, Fuchs H, Kittelmann W, editors. Nonwoven fabrics: raw materials, manufacture, applications, characteristics, testing processes. New York: Wiley; 2006.
2. Wegener R, Marheineke N, Hietel D. Virtual production of filaments and fleece. In: Neunzert H, Prätzel-Wolters D, editors. Currents in industrial mathematics: from concepts to research to education. Berlin: Springer; 2015. p. 103-62.
3. Klar A, Marheineke N, Wegener R. Hierarchy of mathematical models for production processes of technical textiles. Z Angew Math Mech. 2009;89:941-61.
4. Marheineke N, Wegener R. Fiber dynamics in turbulent flows: general modeling framework. SIAM J Appl Math. 2006;66(5):1703-26.
5. Marheineke N, Wegener R. Modeling and application of a stochastic drag for fiber dynamics in turbulent flows. Int J Multiph Flow. 2011;37:136-48.
6. Götz T, Klar A, Marheineke N, Wegener R. A stochastic model and associated Fokker-Planck equation for the fiber lay-down process in nonwoven production processes. SIAM J Appl Math. 2007;67(6):1704-17.
7. Klar A, Maringer J, Wegener R. A smooth 3D model for fiber lay-down in nonwoven production processes. Kinet Relat Models. 2012;5(1):57-112.
8. Doulbeault J, Klar A, Mouhot C, Schmeiser C. Exponential rate of convergence to equilibrium for a model describing fiber lay-down processes. Appl Math Res Express. 2013;2013:165-75.
9. Grothaus M, Klar A. Ergodicity and rate of convergence for a non-sectorial fiber lay-down process. SIAM J Math Anal. 2008;40(3):968-83.
10. Kolb M, Savov M, Wübker A. (Non-)ergodicity of a degenerate diffusion modeling the fiber lay down process. SIAM J Math Anal. 2013;45(1):1-13.
11. Grothaus M, Klar A, Maringer J, Stilgenbauer P, Wegener R. Application of a three-dimensional fiber lay-down model to non-woven production processes. J Math Ind 2014;4:4.
12. Briane M. Three models of nonperiodic fibrous materials obtained by homogenization. Modél Math Anal Numér. 1993;27(6):759-75.
13. Le Bris C. Some numerical approaches for weakly random homogenization. In: Kreiss G, Lötstedt P, Malqvist A, Neytcheva M, editors. Numerical mathematics and advanced applications 2009. Berlin: Springer; 2010. p. 29-45.
14. Lebée A, Sab K. Homogenization of a space frame as a thick plate: application of the bending-gradient theory to a beam lattice. Comput Struct. 2013;127:88-101.
15. Sigmund O. Materials with prescribed constitutive parameters: an inverse homogenization problem. Int J Solids Struct. 1994;31(17):2313-29.
16. Raina A, Linder C. A homogenization approach for nonwoven materials based on fiber undulations and reorientation. J Mech Phys Solids. 2014;65:12-34.
17. Adanur S, Liao T. Fiber arrangement characteristics and their effects on nonwoven tensile behavior. Tex Res J. 1999;69(11):816-24.
18. Bais-Singh S, Goswami BC. Theoretical determination of the mechanical response of spun-bonded nonwovens. J Text Inst. 1995;186(2):271-88.
19. Farukh F, Demirci E, Sabuncuoglu B, Acar M, Pourdeyhimi B, Silberschmidt VV. Mechanical analysis of bi-component-fibre nonwovens: finite-element strategy. Composites, Part B, Eng. 2015;68:327-35.
20. Glowinski R, Pan TW, Hesla TI, Joseph DD, Périaux J. A fictitious domain approach to the direct numerical simulation of incompressible viscous flow past moving rigid bodies: application to particulate flow. J Comput Phys. 2001;169:363-426.
21. Hämäläinen J, Lindström SB, Hämäläinen T, Niskanen H. Papermaking fibre-suspension flow simulations at multiple scales. J Eng Math. 2011;71(1):55-79.
22. Hu HH, Patanker NA, Zhu MY. Direct numerical simulation of fluid-solid systems using arbitrary Lagrangian-Eulerian technique. J Comput Phys. 2001;169:427-62.
23. Peskin CS. The immersed boundary method. Acta Numer. 2002;11:479-517.
24. Stockie JM, Green SI. Simulating the motion of flexible pulp fibres using the immersed boundary method. J Comput Phys. 1998;147(1):147-65.
25. Svenning E, Mark A, Edelvik F, Glatt E, Rief S, Wiegmann A, Martinsson L, Lai R, Fredlund M, Nyman U. Multiphase simulation of fiber suspension flows using immersed boundary methods. Nord Pulp Pap Res J. 2012;27(2):184-91.
26. Tornberg AK, Shelle MJ. Simulating the dynamics and interactions of flexible fibers in Stokes flow. J Comput Phys. 2004;196:8-40.
27. Barrett JW, Knezevic DJ, Süli E. Kinetic models of dilute polymers: analysis, approximation and computation. Prague: Nećas Center for Mathematical Modeling; 2009.
28. Gidaspow D. Multiphase flow and fluidization: continuum and kinetic theory descriptions. San Diego: Academic Press; 1994.
29. Antman SS. Nonlinear problems of elasticity. New York: Springer; 2006.
30. Baus F, Klar A, Marheineke N, Wegener R. Low-Mach-number - slenderness limit for elastic rods. 2015. arXiv:1507.03432.
31. Lindner F, Marheineke N, Stroot H, Vibe A, Wegener R. Stochastic dynamics for inextensible fibers in a spatially semi-discrete setting. Stoch Dyn. 2016. doi:10.1142/S0219437175001622016.
32. Schmeisser A, Wegener R, Hietel D, Hagen H. Smooth convolution-based distance functions. Graph Models. 2015;82:67-76.
33. Scott DW. Multivariate density estimation: theory, practice and visualization. New York: Wiley; 1992.
34. Klar A, Maringer J, Wegener R. A 3D model for fiber lay-down in nonwoven production processes. Math Models Methods Appl Sci. 2012;22(9):1250020.

35. Lagnese J, Leugering G, Schmidt E. Modeling, analysis and control of dynamic elastic multi-link structures. Boston: Springer; 1994.
36. Hohe J, Becker W. Determination of the elasticity tensor of non-orthotropic celluar sandwich cores. Tech Mech. 1999;19(4):259-68.
37. Munoz Romero J. Finite-element analysis of flexible mechanisms using the master-slave approach with emphasis on the modelling of joints [PhD thesis]. London: Imperial College; 2004.
38. Bonilla LL, Götz T, Klar A, Marheineke N, Wegener R. Hydrodynamic limit for the Fokker-Planck equation describing fiber lay-down models. SIAM J Appl Math. 2007;68(3):648-65.
39. Chang C, Gorissen B, Melchior S. Fast oriented bounding box optimization on the rotation group $SO(3,\mathbb{R})$. ACM Trans Graph. 2011;30(5):122.
40. Ericson E. Real-time collision detection. London: CRC Press; 2004.
41. Simo JC. A finite strain beam formulation. The three-dimensional dynamic problem - part I. Comput Methods Appl Mech Eng. 1985;49:55-70.
42. Hill R. Elastic properties of reinforced solids: some theoretical principles. J Mech Phys Solids. 1963;11(5):357-72.
43. Ohser J, Schladitz K. 3D images of materials structures - processing and analysis. Weinheim: Wiley-VCH; 2009.
44. Redenbach C, Rack A, Schladitz K, Wirjadi O, Godehardt M. Beyond imaging: on the quantitative analysis of tomographic volume data. Int J Mater Res. 2012;2:217-27.